Journal of ELECTRONIC MATERIALS, Vol. 47, No. 2, 2018
DOI: 10.1007/s11664-017-5889-7

Structural, Magnetic and Microwave Absorption Properties of Hydrothermally Synthesized (Gd, Mn, Co) Substituted Ba-Hexaferrite Nanoparticles

Z. TORABI,[1] A. ARAB,[1,3] and F. GHANBARI[2]

1.—Department of Physics, Malek Ashtar University of Technology, Shahinshahr, Isfahan, Iran. 2.—Vehicle Technology Developing Center, Tehran, Iran. 3.—e-mail: aa.arab@yahoo.com

Gd, Mn and Co substituted barium hexagonal ferrite nanoparticles, according to the formula $Ba_{1-x}Gd_xFe_{12-2y}(MnCo)_yO_{19}$ and the proportion of $y = \frac{x}{2}$ (and x = 0, 0.1, 0.3, 0.5, 0.7, 0.9, 1), have been prepared by hydrothermal method. Structural, magnetic and absorption microwave properties of the compositions were evaluated by x-ray diffraction (XRD), field-emission scanning electron microscopy (FE-SEM), vibrating sample magnetometry, and vector network analysis. Studying the XRDs data showed the single-phase structure of all samples without any impurities at 900°C calcination temperature. FE-SEM micrographs demonstrated that the morphology of the nanoparticles has planar and nearly hexagonal morphology. The nanoparticles size calculated within the range of 62–85 nm. Study of the room temperature hysteresis loops of calcined samples indicated that maximum magnetizations and coercivities decreased compared to undoped composite with respect to x. The alterations of magnetizations and coercivities are related to the site occupation of substituted ions, change in grain growth inhibition and the effect of spin canting. Moreover, the results of microwave absorption measurements demonstrated that the maximum reflection loss of substituted Ba-hexaferrite equivalent to − 47 dB in sample x = 0.5 with thickness 5.6 mm at a frequency about 17.2 GHz and a bandwidth of 2 GHz greater than − 10 dB. The results showed that Gd has good potential for use as a rare-earth substitution in permanent magnet hexaferrites and these composites can be employed as absorbers in the gigahertz frequency range.

Key words: Nanoparticles, barium hexaferrite, microwave absorption, hydrothermal method

INTRODUCTION

Ba-hexaferrite with magnetoplumbite structure is a hard magnetic material.[1,2] These materials have a very large saturation magnetization (M_s), remnant magnetization (M_r) and high coercivity (H_c) due to strong uniaxial magneto-crystalline anisotropy, which has been widely used as permanent magnets, injection-molded pieces, microwave device, and magnetic recording media.[3–8]

(Received June 25, 2017; accepted October 23, 2017; published online November 9, 2017)

The development of microwave electronic devices has led to improvement of electromagnetic absorber technology and promoted the research into absorption of electromagnetic radiation. Ba-hexaferrite nanoparticles have large electrical resistivity and high microwave magnetic losses, so is a favorite filler for absorption of gigahertz frequencies.[7]

Several processes have been proposed, such as the mechanical milling method,[5,6] sol–gel method,[8] Co-precipitation method,[9,10] and hydrothermal method.[11,12] For such an application, control of the particle size and shape is very important. Therefore, an interesting goal is synthesizing procedures

permitting easy control of the particle size without any chemicals appearing that are not in the final formulation. The properties of nanoparticles depend on the synthesis procedure; therefore, it has particular importance. The production of nanoparticles with high purity and a more uniform particle size leads to the improvement of structural and magnetic properties. Hydrothermal method in comparison to the other methods is more acceptable since the size of nanoparticles and chemical combinations are better controlled, and the phase formation temperature is lower.[13]

In the production process by hydrothermal method, enclosed environment with pressure is used, so the required temperature for the formation of hexaferrite nanoparticle phrase is reduced. Another advantage of this method compared to the other chemical methods is that, regarding the conditions of making samples in enclosed environment, the evaporation of volatile elements and the changes in stoichiometric in production process is impossible.

Different reports have shown the substitution of elements such as Co^{2+}, Co^{2+}-Ti^{4+}, Mg^{2+}-Zr^{4+}, Zn^{2+}-Sn^{2+}, Zr^{4+}-Co^{2+}[6–10] and trivalent elements such as Al^{3+}, Cr^{3+}, Gd^{3+}[11–13] in the M-type hexaferrite structure. The selection of substituted cations in the M-type hexaferrite structure must decrease the resonance frequency, and furthermore maintain the magnetic properties of this strong absorbent. M-type hexaferrites include 24 ions. These iron ions are distributed in five lattice positions. These positions consist of three octahedral sites 12k, 2a and $4f_2$, one tetrahedral site $4f_1$ and a bi-pyramidal triangular position 2b. It is noteworthy that 12k, 2a and 2b have a high torque spin, whereas $4f_1$ and $4f_2$ have low torque spin.[14] Therefore, in this study we attempted to synthesize $Ba_{1-x}Gd_xFe_{12-2y}(MnCo)_yO_{19}$ (x = 0, 0.1, 03, 0.5, 0.7, 0.9, 1) nanoparticles by the hydrothermal method, and effects of simultaneous substitution of two and trivalent cations Co2+, Mn2+ and Gd3+ have been studied on structural, magnetic and absorption of microwave radiations of barium hexaferrite nanoparticles. Also, the trend of changes from barium ferrite to gadolinium ferrite and characterizations with a new series of substitutions were compared to previous works in order to recognize its microwave applications in the electronics and telecommunications industries such as radars, phase shifters, circulators.

EXPERIMENTAL

First, to produce samples of $BaFe_{12}O_{19}$, aqueous mixtures of barium (II) nitrate ($Ba(No_3)_2$), iron (III) nitrate ($Fe(NO_3)_3$) and NaOH solution (0.98 M) were prepared by the hydrothermal method. The resulting suspensions were sealed in an autoclave cell and heated for the required duration and then cooled to room temperature. To produce powders, the suspension was washed repeatedly using deionized water until no NaCl was detectable, dried at 100 in an oven, calcined at 800°C, 900°C, and 1000°C for 2 h at a heating rate of 10°C/min and then free cooled to room temperature.

The starting materials used for preparation of the samples were $Fe(NO_3)_3.9H_2O$ (Merck, 98%), $Ba(No_3)_2$ (Merck, 99%), Gd $(NO_3)_3.6H_2O$ (Aldrovich, 99.5%), $Mn(NO_3)_2.4H_2O$ (Merck, 98.5%), $Co(NO_3)_2.6H_2O$ (99%) and NaOH (Merck, 99%). In a typical experimental procedure, stoichiometric aqueous mixtures of barium nitrate ($Ba(No_3)_2$), cobalt nitrate ($Co(NO3)_2$), manganese nitrate ($Mn(NO_3)_2$), gadolinium nitrate ($Gd(NO_3)_3$) and iron nitrate ($Fe(NO3)_3$) were prepared with a total concentration of 0.1 mol L^{-1}. These materials are mixed in compositions of Ba:(Fe + Mn + Gd + Co) = 1:12 with the nominal formula of $Ba_{1-x}Gd_x Fe_{12-2y}(MnCo)_yO_{19}$ and a ratio of $y = \frac{x}{2}$, where x is equal to 0, 0.1, 0.3, 0.5, 0.7, 0.9 and 1, prepared by the hydrothermal method. Stoichiometric amounts of the metal salts were weighed and mixed with distilled water for 30 min. Sodium hydroxide (NaOH) solution (0.98 M) as a precipitating agent was then added dropwise to the mixture to adjust the solution pH to 12 under vigorous stirring. At the same time the solution containing the precipitate was stirred for 2 h. The resulting suspensions were sealed in an autoclave cell at 200°C for 7 h and heated for the required duration and then cooled to room temperature. Finally to produce powders, the precipitates were washed three times with water by centrifuge to reduce the pH to 7 and remove remaining NaCl and NaOH, then dried at 100°C in an oven and calcined at 900°C in a programmed furnace for 2 h at a heating rate of 10°C/min and then free-cooled to room temperature. X-ray diffraction (XRD) analysis was performed to confirm the phase formation of hexaferrites by use of a PANalytical Pro MPD-X'pert HighScore XRD instrument using CuKα radiation (λ = 1.5406 Å).

The lattice parameters of the single phase hexaferrites were determined from the XRD data, and the microstructures were characterized by field-emission scanning electron microscopy (FE-SEM) (Hitachi S-4160). The mean crystallite sizes were calculated from the full-width at half maximum (FWHM) of the peaks, using Scherrer's formula and were compared to FE-SEM images. The room temperature hysteresis loops were studied in a maximum field of 15 kOe by VSM (MDKB-Iran). Magnetizations and coercivities of the samples were then obtained from the loops. The average crystallites sizes of samples were calculated from XRD data by Scherer's formula. The lattice parameters are calculated by use of appropriate equation[15]:

$$d = \frac{1}{\sqrt{\frac{4}{3}\frac{h^2+hk+k^2}{a^2} + \frac{l^2}{c^2}}} \quad (1)$$

where "d" is the distance between two crystallographic planes (hkl), "a" and "c" are the unit cell parameters. Finally, to study the microwave absorption characteristics of Ba-hexaferrite nanoparticles,

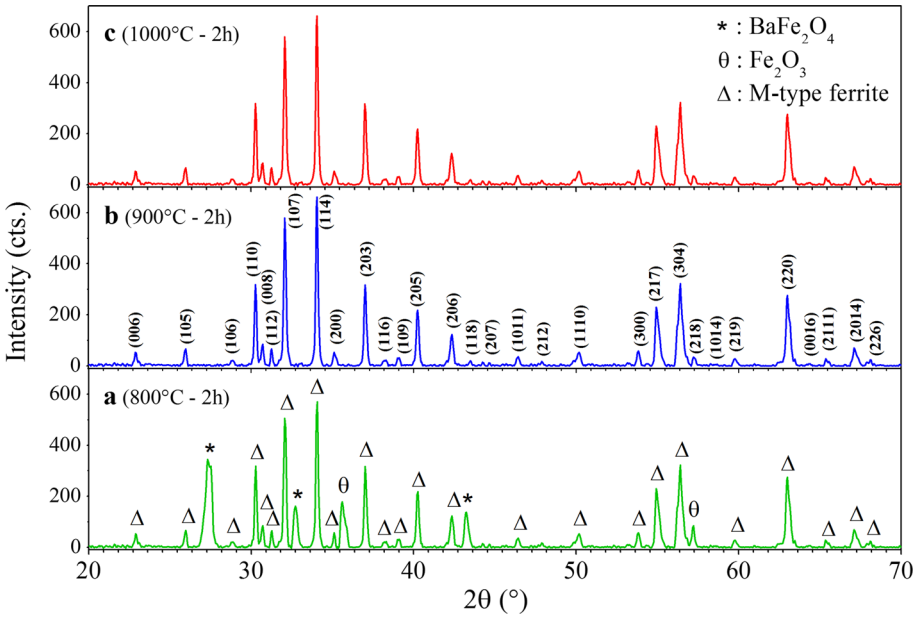

Fig. 1. X-ray diffraction patterns of Ba-hexaferrite ($BaFe_{12}O_{19}$) with different calcination temperatures (a) 800°C, (b) 900°C, and (c) 1000°C.

VNA (HP 84100C) was used. For this purpose, the hollow pills were prepared by mixing ferrite powders and paraffin with a weight percentage of 70:30 and then pressed to form a coaxial-shape with an inner diameter of 2 mm, an outer diameter of 7 mm and a thicknesses of 2 mm, for calculating the real and imaginary values of permittivity (ε) and permeability (μ) in the range of 2–18 GHz by VNA. Then reflection losses were calculated with Eqs. 2 and 3. The normalized input impedance (Z_{in}) of a microwave absorbing layer returned by a reflector is shown by:

$$Z_{in} = \frac{Z_i}{Z_o} = \left(\frac{\mu_r}{\varepsilon_r}\right)^{0.5} \tanh\left[\frac{j2\pi(\mu_r\varepsilon_r)^{0.5} fd}{c}\right] \quad (2)$$

where Z_{in} is the normalized input impedance at the absorber surface, Z_i is the input impedance, and Z_o is the impedance of free space, μ_r and ε_r are relative permeability and permittivity of the medium, respectively, f is the frequency of microwaves in free space, C is the velocity of the electromagnetic wave, and d is the thickness of absorber. Reflection loss, the ratio of reflected power to incident power, is related to Z_{in} as is shown:[16]

$$\text{Reflection loss(dB)} = 20\log_{10}\left[\frac{(Z_{in}-1)}{(Z_{in}+1)}\right] \quad (3)$$

RESULTS AND DISCUSSION

Structural and Morphological Evaluation

Figure 1 shows the XRD patterns of Ba-hexagonal ferrites calcined at 800°C, 900°C, and 1000°C. According to this figure, the calcined sample at 800°C has impurity phases α-Fe_2O_3, spinel ferrite middle phase $BaFe_2O_4$ and a number of M-type barium hexaferrite phases in comparison to peaks of M-type standard barium hexaferrite with card-number 01-074-1121. The calcination temperature was increased up to 900°C, extra phases were removed gradually, and the pure phase of M-type barium hexaferrite was formed. Increased synthesis temperature led to merging the ferrite spinel middle phase $BaFe_2O_4$ (indexed by *) with hexaferrites structure and dissolves impurity phase α-Fe_2O_3 (indexed by Θ). Therefore, for the calcined hexaferrites, a pure phase at 900°C was formed without any effect of extra phases. The peaks of the calcined sample at 1000°C are in agreement with peaks of the calcined sample at 900°C. All of the shown peaks for samples at 900°C, and 1000°C were identified, and these were adapted to the reference card of the mentioned standard barium hexaferrite.[17] By comparing XRD peaks of the 900°C sample to the peaks of the 1000°C sample, it can be seen that the peaks of the 1000°C sample have a slight increase in severity. Consequently, it can be said that the optimal temperature of phase formation is 900°C.

The values of average crystallites size, lattice parameters and the c/a ratios of the 900°C, and 1000°C samples are shown in Table I. As can be seen from this table, all characters have an increasing trend by increasing calcination temperature. The increase in crystallite size can be related to the formation of agglomerates and by the extensive degree of particle coarsening at higher temperatures.[18] In addition, the crystallite size of the 900°C samples was about 48 nm, which is appropriate for signal-to-noise proportions.[19] Figure 2 shows typical XRD patterns for the calcined pure barium hexaferrite and the substituted ones (x = 0, 0.1, 0.5 and 1) for 2 h at 900°C in air. These patterns are

often conformed to the previously mentioned standard barium hexaferrite with an insignificant amount of impurity phase (* in Fig. 2) as higher substituted, which has no significant effect on the hexaferrite structural properties. Measurements were taken at 20–70 angles, and the average crystallite size and lattice parameters were calculated from XRD data by using Scherer's formula and Eq. 1, respectively. Figure 3 and Table II show the crystallite size, lattice parameters, c/a ratio and the unit cell volume for different substituted values. It is observed that by increasing the substituted values, lattice constant c always has an increasing trend, and the c/a ratio first increased and then decreased by reaching the gadolinium hexaferrites phase. Cations substitution with various radius influences the structural properties. The ionic radius of gadolinium (R_{Gd} = 1.07 Å) is larger than the barium (R_{Ba} = 1.35 Å).[20] In addition, ionic radius of iron (R_{Fe} = 0.64 Å) is smaller than cobalt (R_{Co} = 0.74 Å) and manganese (R_{Mn} = 0.81 Å). Cation substitution in the hexaferrite structure leads to an increase in the lattice parameter c and the c/a ratio.

Figure 4 shows FE-SEM micrographs of the selected sample (x = 0). By increasing calcination temperature, the particle size has grown and morphology has changed. The morphology of particles for the calcined sample at a temperature of 800°C has a blade shape and is hexagonal. By increasing calcination temperature to 900°C the particles grown are often hexagonal and planar shape. Increasing calcination temperature up to 1000°C leads to more growth of particles in various crystallographic directions, and the morphology of particles has been in the form of a large, planar blade and is chaotic. In addition, Fig. 5 shows FE-SEM micrographs of the substituted samples at x different values calcined at 900°C. In the FE-SEM images, both micrometer and nanometer range of grains are observable, but at higher magnifications, noticing details shows that all present properties are confirming to finer grains. By increasing the value of substitutions the size range of the particles had negligible changes and morphology of the

Table I. Crystallite size, lattice parameters and c/a ratio for $BaFe_{12}O_{19}$ nanoparticles synthesized at (a) 800°C, (b) 900°C, and (c) 1000°C

The sintering temperature	(b) 900°C	(c) 1000°C
Annealing time (h)	2	2
Average crystallite size (D(nm))	48.4	52.34
Lattice parameters (a(Å))	5.91	5.93
Lattice parameters (c(Å))	23.28	23.92
c/a	3.93	4.03

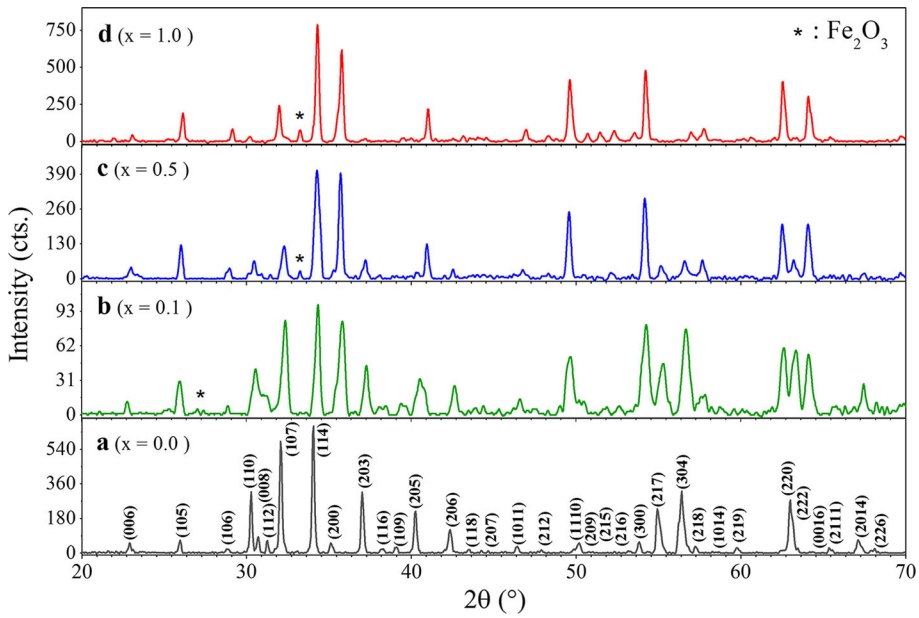

Fig. 2. X-ray diffraction patterns of $Ba_{1-x}Gd_xFe_{12-2y}(MnCo)_yO_{19}$ at 900°C for $y = \frac{x}{2}$ and different x values (a) 0, (b) 0.1, (c) 0.5, and (d) 1.

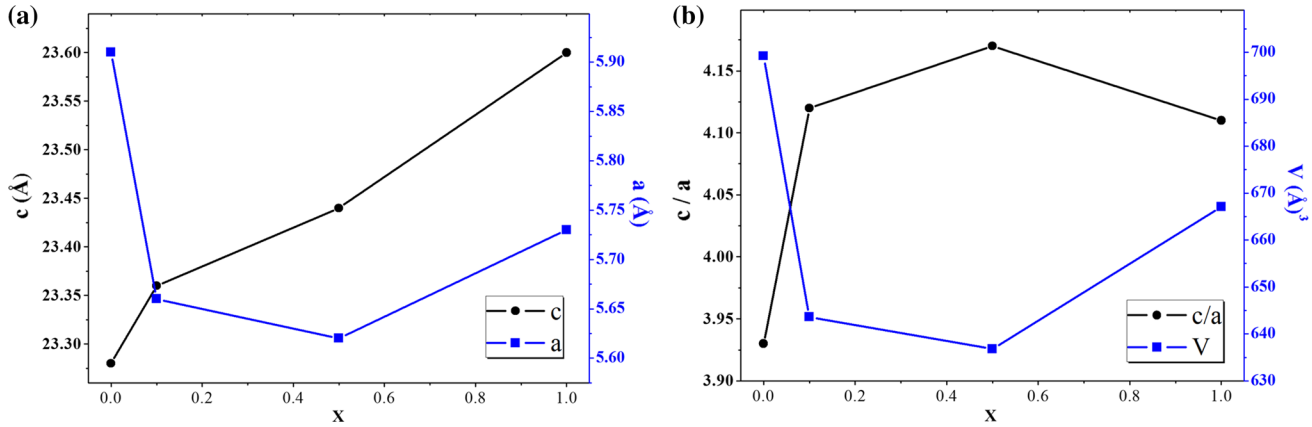

Fig. 3. The variations of structural parameters in $Ba_{1-x}Gd_xFe_{12-2y}(MnCo)_yO_{19}$ for $y = \frac{x}{2}$ and x = 0, 0.1, 0.5 and 1, (a) lattice parameters "*a*" and "*c*", (b) *c/a* ratio and unit cell volume.

Table II. Crystallite size, lattice parameters and *c/a* ratio of *x* = 0, 0.1, 0.5 and 1

	***X* = 0**	***X* = 0.1**	***x* = 0.5**	***x* = 1.0**
Average crystallite size [*D*(nm)]	48.4	42.45	44.35	46.36
Lattice parameter (*a*(Å))	5.91	5.66	5.62	5.73
Lattice parameter (*c*(Å))	23.28	23.36	23.44	23.60
c / *a*	3.93	4.12	4.17	4.11
V (Å)^3	699.2	643.6	636.8	667.1

nanoparticles have not had significant changes, and it can be said that the particles have had almost the same morphologies. Plane and hexagonal morphologies can be seen in this figure. The range of particle size has almost been low and is placed in the range of 62–85 nm. Preparing nanoparticles by the hydrothermal method makes it possible to have availability to particles with analogous morphology and it also gives the approximate size of the particles. The calcination process is effective in the growth of the particles. It can be claimed that the calcination process provides the required activation energy for interaction and growth of the nanoparticles and leads to the growth of particles.[21,22]

Magnetic Properties

Figure 6a shows the magnetic hysteresis loops for the calcined Ba-hexagonal ferrites at 800°C, 900°C, and 1000°C different temperatures. The values of maximum magnetization (M_{max}), remnant magnetization (M_r) and coercivity (H_c) of the calcined sample at 800°C are determined from hysteresis loop curve and these values are 38.7 emu/g, 17.48 emu/g and 2254 Oe, respectively. As observed in XRD patterns, the presence of middle phases and impurities near the M-type hexaferrite phase indicate the impurity of the composition, and it has affected the magnetic parameters. The visible butterfly-shape in Fig. 6a, for sample a (800°C), is due to the secondary impurity phases appearing in the sample, which is compatible with its XRD results (Fig. 1). Appearance of impurities will change the crystalline structure and thus the magneto-crystalline anisotropy. The shape anisotropy, apart from two other types of anisotropy, i.e. magneto-crystalline and stress or residual stress, are considered to be the reason for the butterfly-shaped hysteresis loop.[23] By increasing the calcination temperature up to 900°C, the hysteresis loop would be completely symmetric, and regarding the XRD pattern for this sample, a single-phase M-type hexaferrite was gained as a result. Maximum and remnant magnetizations and the coercivity of this sample are 41.74 emu/g, 25.08 emu/g and 3371 Oe, respectively. Finally, by increasing the calcination temperature up to 1000°C, maximum and remnant magnetizations and the coercivity of this sample changes to 45.64 emu/g, 26.27 emu/g and 2184 Oe, respectively. The increase in magnetization in the last sample is due to the increase of crystallinity. To study the magnetic properties, important parameters such as the particle size and magneto-crystalline anisotropy should be studied and considered. In the multi-domain magnetic nanoparticles, there is a reverse relation between the particle size and the coercivity.[24] As observed in the FE-SEM micrographs, the particle size is increased by increasing the calcining temperature, and therefore, coercivity is increased by forming a Ba-hexaferrite phase for the sample calcined at 900°C, but it decreases after

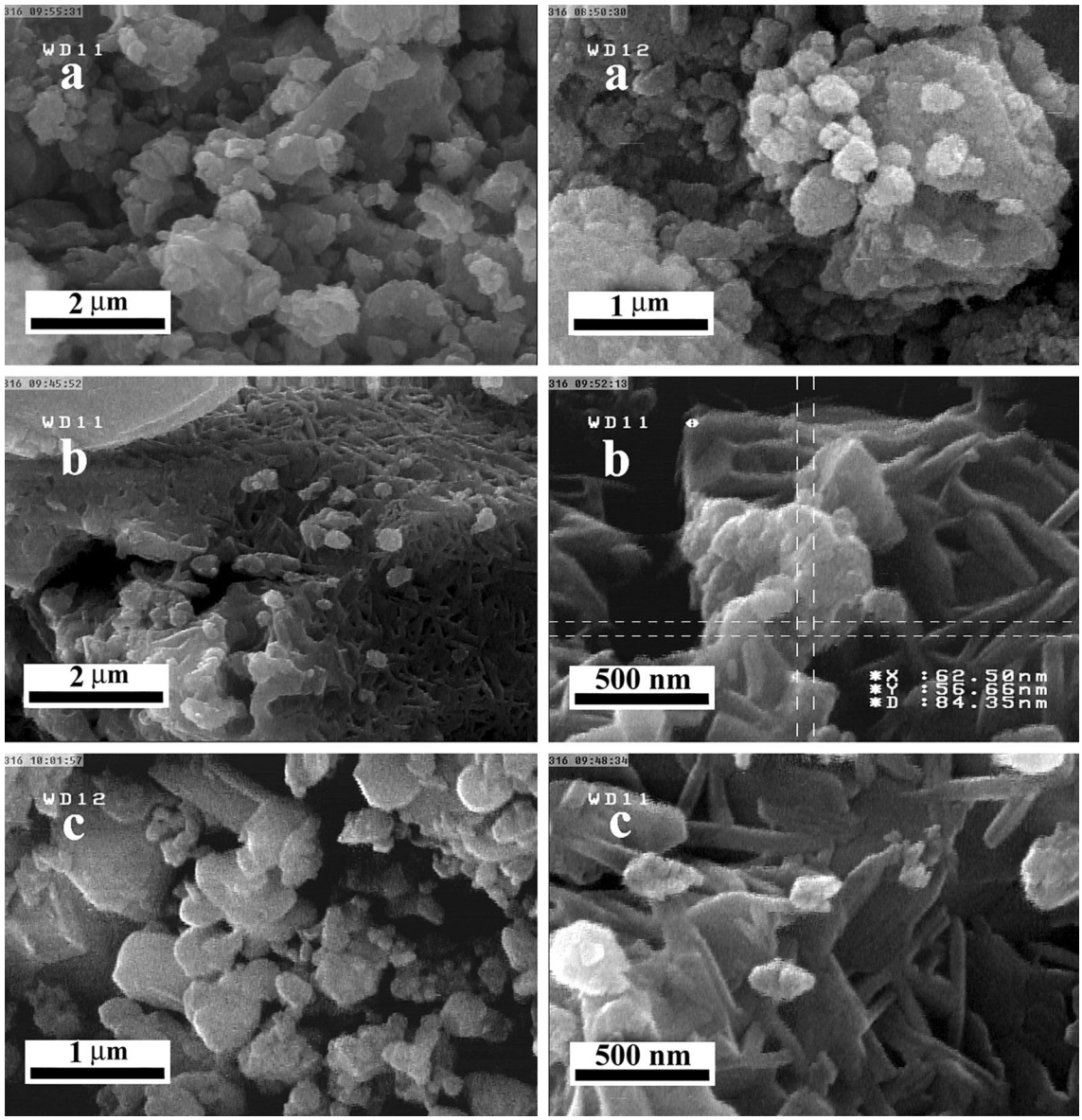

Fig. 4. FE-SEM micrographs of $BaFe_{12}O_{19}$ with different calcination temperatures (a) 800°C, (b) 900°C, and (c) 1000°C.

that for the sample calcined at 1000°C. Coercivities have slightly gone up with increasing temperature, due to an increase of separations between magnetic grains because of lowering magnetostatic interactions (Fig. 6a).[25] Figure 6b shows the room temperature magnetic hysteresis loops for all the substituted samples. The estimated values of M_{max} and H_c are shown in Fig. 7. The hysteresis loops of samples were obtained by VSM technique at 300 k and maximum applied magnetic field of 15 KOe. As seen in Table III, by increasing the value of substitution, the M_{max} values decreased to the $x = 0.5$ sample and were measured as 6.48 emu/g. Also, with further substitutions, the M_{max} process showed an increasing trend, and for the $x = 1$ sample attained $M_{max} = 17.63$ emu/g. Coercivity of pure ferrite barium decreased from 4471 Oe to 1041 Oe for the $x = 0.3$ sample. Then, with more substitutions until $x = 0.7$, a value of 1224 Oe was gained. Finally, the decreasing trend to the $x = 1$ sample was attained in 775 Oe. Chemical composition, reposition of the cations, production method and the temperature of formation phase are among the most significant factors influencing the magnetization and the coercivity.[26]

Regarding to Co^{2+} ($3\mu_B$) and Mn^{2+} ($5\mu_B$) magnetic moments, if Co^{2+} substitutes in 12k, 2a and 2b, the net number of upward torques would decrease resulting in a decrease at magnetization, as respects if Co^{2+} substitutes in $4f_1$ and $4f_2$, the downward ones increase, and thus the magnetization increases, which is the inverse for Mn^{2+}. Furthermore, these substitutions weaken the superexchange interaction between Fe^{3+} cations in the tetrahedral and

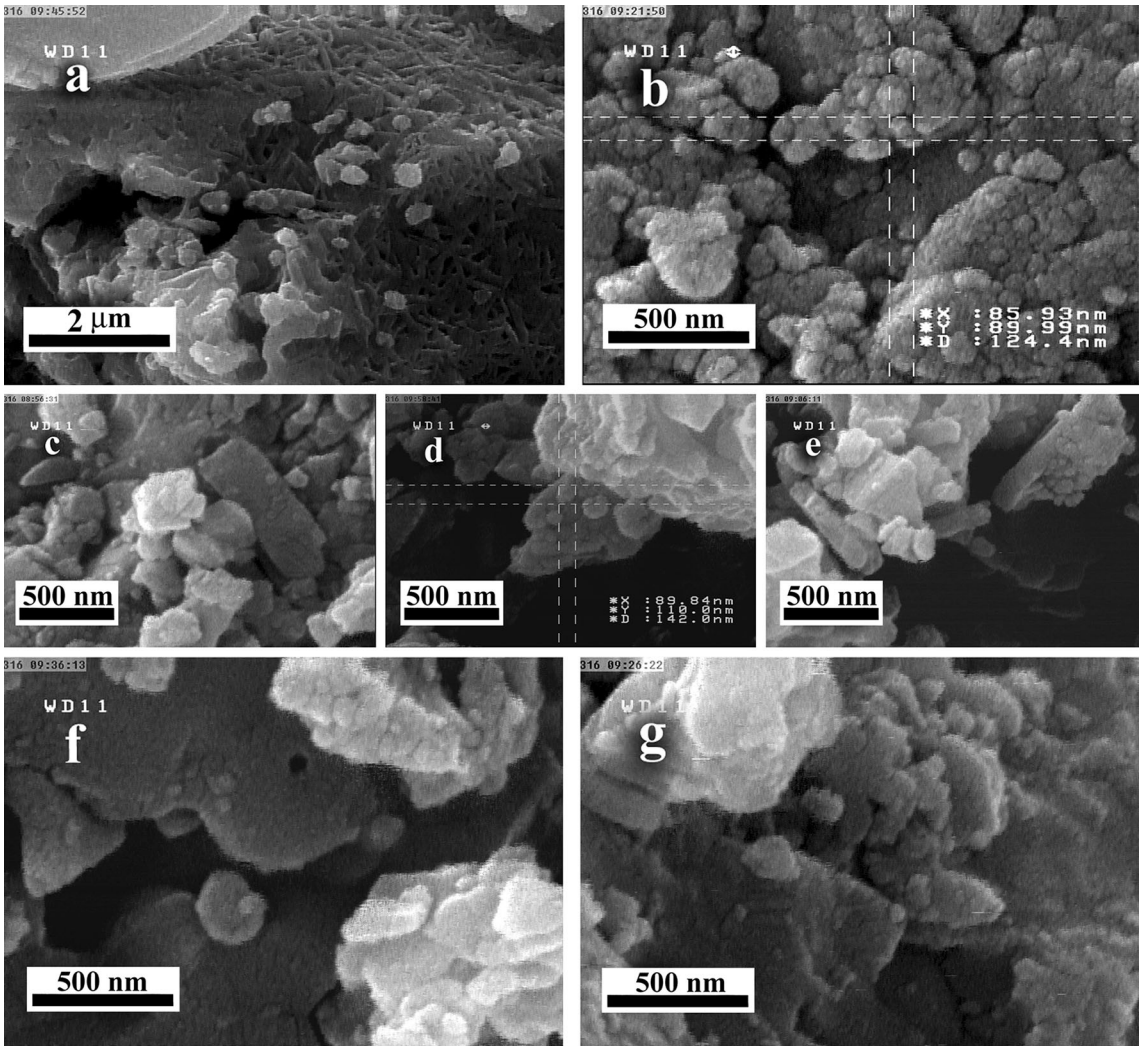

Fig. 5. FE-SEM micrographs showing the hydrothermally synthesized $Ba_{1-x}Gd_xFe_{12-2x}(MnCo)_xO_{19}$ powders for $y = \frac{x}{2}$ and different x values (a) 0, (b) 0.1, (c) 0.3, (d) 0.5, (e) 0.7, (f) 0.9, and (g) 1.

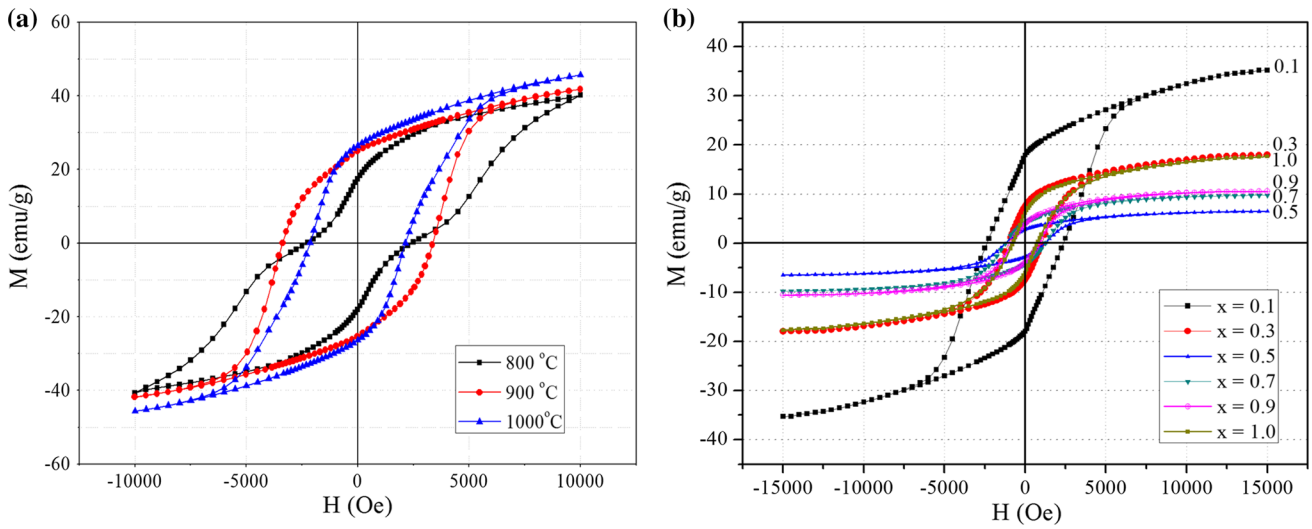

Fig. 6. Magnetic hysteresis loops (a) $BaFe_{12}O_{19}$ at calcination temperatures 800°C, 900°C, and 1000°C, (b) $Ba_{1-x}Gd_xFe_{12-2y}(MnCo)_yO_{19}$ for $y = \frac{x}{2}$ and x from 0.1 to 1.

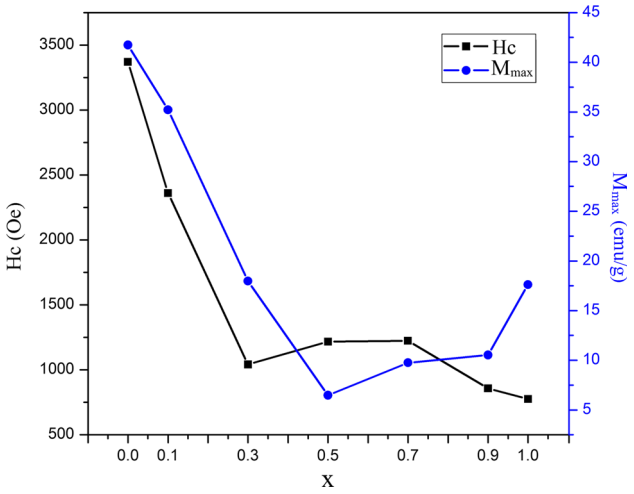

Fig. 7. The variations of the coercivity and maximum magnetization versus substitution values x of $Ba_{1-x}Gd_xFe_{12-2y}(MnCo)_yO_{19}$ for $y = \frac{x}{2}$ and x = 0–1.

Table III. The variations of the maximum and remnant magnetizations, coercivity and maximum applied field for $Ba_{1-x}Gd_xFe_{12-2y}(MnCo)_yO_{19}$ for $y = \frac{x}{2}$ and x = 0–1

	M_{max} (emu/g)	M_r (emu/g)	H_C (Oe)	H_{max} (KOe)
x = 0	41.74	25.08	3371	10
x = 0.1	35.21	18.62	2361	15
x = 0.3	17.97	9.43	1041	15
x = 0.5	6.48	4.54	1217	15
x = 0.7	9.75	5.34	1224	15
x = 0.9	10.53	5.88	858	15
x = 1	17.63	9.44	775	15

octahedral sites and, consequently, reduce the magnetization. The Bohr magneton value of replaced cations must be noticed. The replacement of substituted cations in the hexaferrite structure weakens or strengthens interactions among magnetic ions and affects the magnetization based on their situation. High coercivity besides fine-particles for Ba-hexaferrite shows a significant improvement in comparison to the other report.[24,27] It should be noted that positioning Mn^{2+} and Co^{2+} cations in lieu of Fe^{3+} along with Gd^{3+} instead of Ba^{2+} will keep charge balance of all pure and substituted samples, but spin canting may occur due to difference between Fe^{3+} and Mn^{2+}-Co^{2+} magnetic moments which results in lowering magnetizations in substituted samples.

Coercivity can be influenced by such parameters as shape anisotropy, particle size and magneto-crystalline anisotropy. Referring to the FE-SEM pictures, we observed that particle morphology has almost been monotonous, and the effect of shape anisotropy is so negligible it can be ignored. The particle size has changed a little and has partially affected the magnetic properties. Dependence of coercivity to the magneto-crystalline anisotropy constant is direct while is reverse to the particle size. So changes in coercivity and the magneto-crystalline anisotropy constant are caused by substitution of manganese, cobalt and gadolinium ions. As a result, in most of the combination, these substitutions have led to a decrease in the magneto-crystalline anisotropy constant. Furthermore, it shows the dominant influence of some of the substituted cations and this results in a decrease in coercivity.[24,26] The previous reports confirm that usually both magnetic and nonmagnetic cations substitutions cause a decrease in coercivity and magneto-crystalline anisotropy. The 12k, 2a and $4f_2$ sites have the most influence on the magneto-crystalline constants because of their intensive superexchange interactions in M-type hexaferrites. It is useful to note that by the substitution of iron cations at the 12k and 2a positions, a displacement for $4f_2$ will occur, which causes a decrease of magneto-crystalline constants and coercivity.[27–29]

Also, it seems that Gd acts as a grain growth inhibitor, especially for a certain concentration, thus reaching higher coercivity for samples with x = 0.3–0.7. This can be mentioned as an external effect of Gd on the microstructure of the Gd materials, directly influencing coercivity. The grain growth prevention effect is not strong in the case of Ba-Gd-MnCo samples, probably related to the presence of Mn and Co, which are liable for the decrease of coercivity values in low concentration of substitutions for x = 0–0.3.[25,30]

Diminution of magnetization can be justified according to site occupations by Gd^{3+}, Co^{2+} and Mn^{2+} ions. For samples with x = 0–1, due to the different ionic radii of Gd^{3+} (0.935 Å) from that of Ba (1.35 Å), Mn^{2+} (0.75 Å) and Co^{2+} (0.983 Å), from that of Fe^{3+} (0.645 Å), a decrease in super-exchange interactions between $4f_1$–12k and $4f_1$–2a is expected, so magnetizations of the samples have changed. It is reported in previous research that Co^{2+} ($3\mu_B$) cations usually occupy 2b and $4f_2$ positions while Mn^{2+} ($5\mu_B$) cations commonly prefer to occupy tetrahedral coordination $4f_1$.[31] Thus, it can be said that substitution of Mn^{2+} cations have caused a decrease in all magnetization in this research. Therefore, it seems that occupation of 2b sites in lower substitution concentration values and $4f_2$ in higher ones by Co^{2+} has decreased and increased magnetizations, respectively.

Microwave Properties

Figure 8 shows the frequency dependencies of the real and imaginary parts of permittivity ($\varepsilon = \varepsilon' - j\varepsilon''$, permeability ($\mu = \mu' - j\mu''$), electric and magnetic loss tangents of the samples, including substituted hexaferrite powders with compositional formulas:

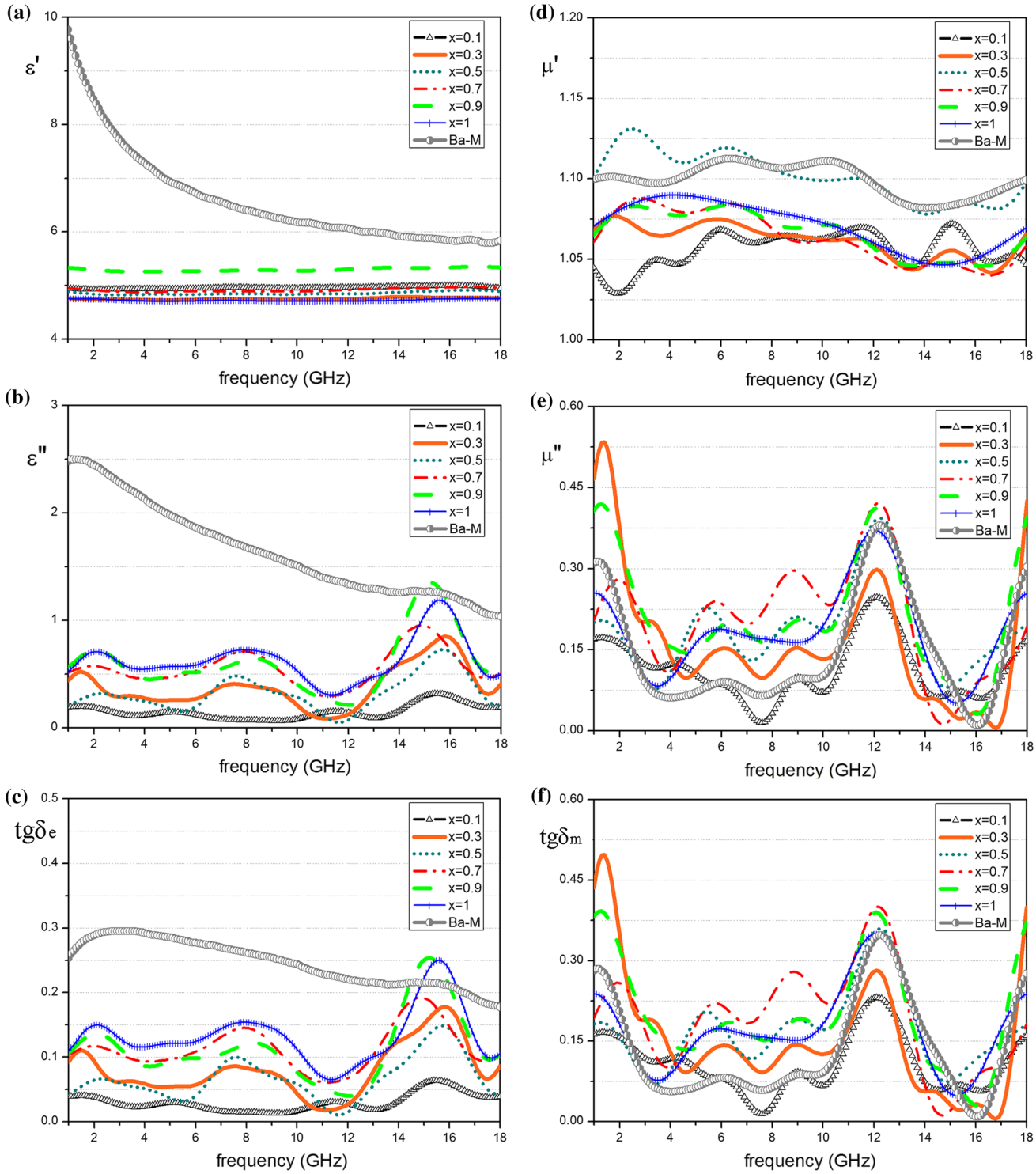

Fig. 8. The frequency dependency curves of $Ba_{1-x}Gd_xFe_{12-2y}(MnCo)_yO_{19}$ containing 70% ferrite for $y = \frac{x}{2}$ and x = 0–1, (a) real permittivity, (b) imaginary permittivity, (c) electric loss tangent, (d) real permeability, (e) imaginary permeability, and (f) magnetic loss tangent.

$Ba_{1-x}Gd_xFe_{12-2y}$ $(MnCo)_yO_{19}$ for x from 0 to 1 and $y = \frac{x}{2}$. There were some oscillating ripples in permittivity and permeability datasets that did not belong to material properties, but were attributed to environmental noises and small volume fraction of ferrite, we balanced them using fast Fourier transform (FFT) filter technique and then plotted to achieve more realistic analysis.

The real part of permittivity (ε') is related to polarization of dipoles and the imaginary part (ε'') to

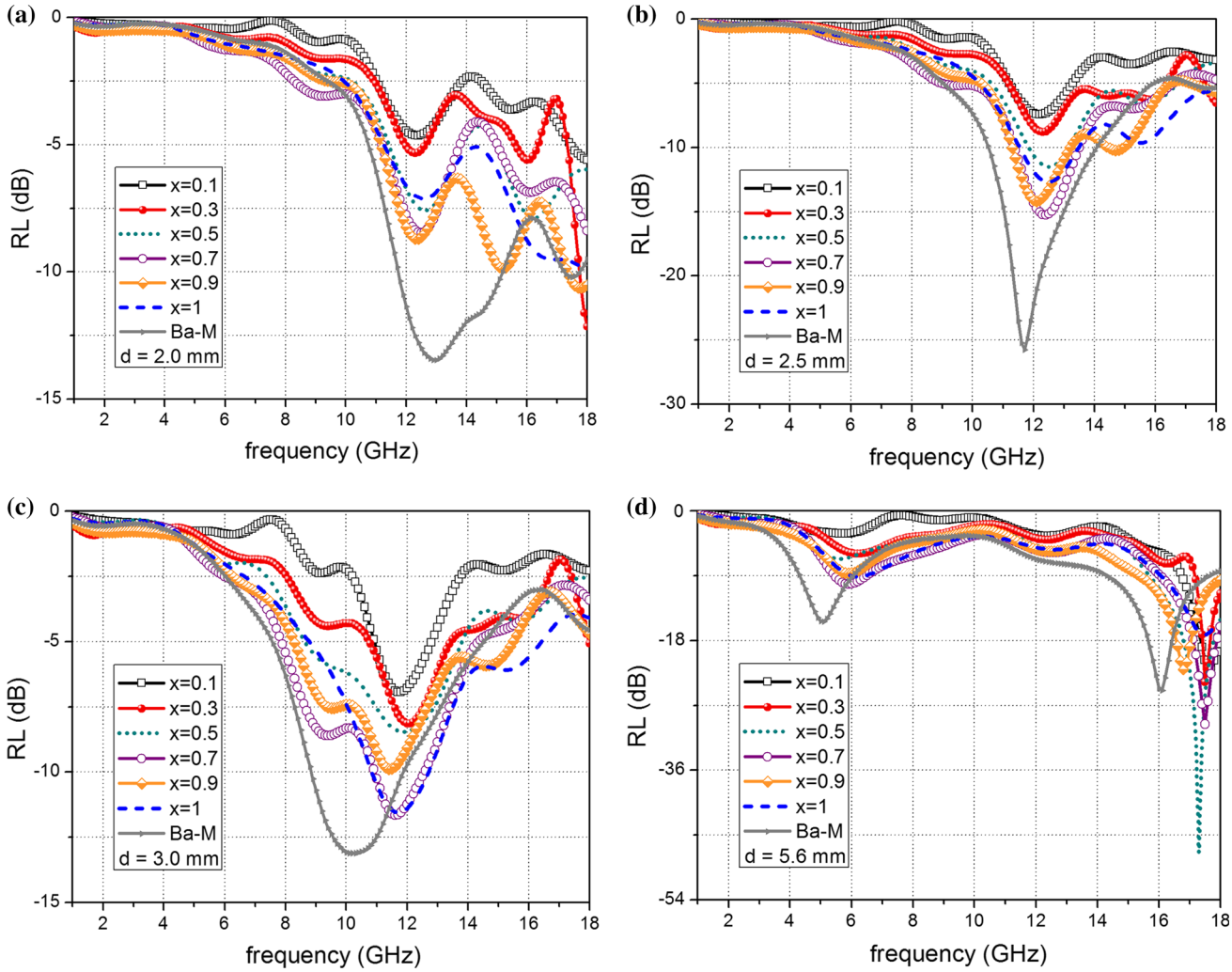

Fig. 9. Reflection loss curves of $Ba_{1-x}Gd_xFe_{12-2y}(MnCo)_yO_{19}$ containing 70% ferrite for $y = \frac{x}{2}$ and x = 0–1 with absorber thicknesses (a) 2 mm, (b) 2.5 mm, (c) 3 mm, and (d) 5.6 mm.

dissipation of electric energy and $tg\delta_e = \frac{\varepsilon''}{\varepsilon'}$ shows the electric loss. A physical interpretation for the peaks in $tg\delta_e$ about 15–16 GHz can be done on the basis of electric dipoles formed by cations Ba^{2+}, $Fe^{3+}$and Gd^{3+} of the structure with their surrounding O^{2-} ions, but the main source of polarization in ferrites is the substitution of Fe^{3+} ions by Mn^{2+} and Co^{2+} ions on octahedral 2a crystallographic sites helping dielectric polarization and relaxation, which has direct influence on ε' (Fig. 8a).[32–35] It was observed that the amplitude of the resonance peaks at about 16 GHz increased with increasing Gd-Mn-Co content up to 0.9, which is because the imaginary permittivity depends on the number and nature of the different ions present in the sample (Fig. 8b). The increase in oscillatory behavior of $tg\delta_e$ (Fig. 8c) for substituted samples compared to pure Ba-M can be justified on the basis of these mentioned phenomena for ε' and ε''.[36] The real part of permeability (μ') is related to magnetization and domain wall displacement, and the imaginary part (μ'') to dissipation of magnetic energy and $tg\delta_m = \frac{\mu''}{\mu'}$ shows the magnetic loss. Substitution of Gd-Mn-Co ions in the Ba-hexaferrite structure may lead to weakening of the Fe^{3+}-O-Fe^{3+} super exchange interaction by changing the lattice parameters and spin canting. This effect correlates with lowering of magnetizations, so a reduction in permeability of substituted samples in comparison to pure sample is expected (Fig. 8d).[34] In Fig. 8e multiple peaks can be ascribed to the phenomenon of ferromagnetic resonances due to Fe^{3+} ions, Mn^{2+} ions, Co^{2+} ions and their coupling. The ferromagnetic resonance frequency of the ferrites can be calculated from the relation:

$$f_r = \left(\frac{\gamma}{2p}\right)\mathrm{Ha} \qquad (4)$$

where Ha is the anisotropy field and γ is the gyromagnetic ratio (1.4 g GHz kOe^{-1}, in which g is the Landé factor, equal to 2 for Fe^{3+} ions, greater than 3 for Mn^{2+} and Co^{2+} ions, and greater than 2

for the coupling). The resonance peaks on the lower side correspond to the ferromagnetic resonance due to Fe^{3+} ions and the peaks on the higher side correspond to the resonance due to coupling between Fe^{3+}, Mn^{2+} and Co^{2+} ions.[36]

Regarding the magnetic loss mechanisms happening at the GHz region in Fig. 8f, all samples follow an increasing trend at frequencies of about 12 GHz, which is imputed to the relaxation phenomena of domain magnetization rotation or domain wall displacement.[37] The rise of magnetization, reflected in loss variation, occurs due to enhanced hyperfine fields at 12k and 2b sites, which strengthen Fe^{3+}-O-Fe^{3+}super exchange interaction,[38,39] although it was observed that the increasing Gd-Mn-Co substitution for Ba^{2+} ions was followed by a decrease of magnetization compared to pure hexaferrite. It is observable in Fig. 8e and f that the amplitude of the resonance peaks near frequency 12 GHz increased with increasing Gd-Mn-Co content up to 0.7, which can be ascribed to the imaginary permeability dependence on the number and nature of the different ions present in the sample just similar to dielectric losses. This amplification in magnetic loss for the substituted ferrites compared with pure BaM is desirable for lossy application goals.

Figure 9 shows the reflection loss charts according to the frequency for all samples and for different values and thicknesses from 2 mm to 3 mm. The resulting data for the reflection loss properties of the substitution samples are listed in Table IV. It can be said that the appearance of two peaks usually occurs in a loss of substituted Ba-hexaferrites, which the first peak caused by resonance in domain wall motion and the second by resonance in the rotation of the magnetization vector.[40] Less than 10 dB absorbing bandwidth means that the frequency band width can attain at least 90% reflection loss. It can be seen that the substitution in Ba-hexaferrites have a countless influence on the microwave absorbing properties. As reported in some research, pure Ba-hexaferrite composition usually does not have an acceptable absorption of electromagnetic waves in this frequency range. Barium hexaferrite can absorb electromagnetic waves of about 48 GHz, and by simultaneous cation substitutions of other cations the ferromagnetic resonance frequencies decreases to the frequency range of 2–18 GHz.[40–42] In this research, intensive reflection loss of pure Ba-hexaferrite is because of the electrical characteristics such as polarization of this sample due to chemical and physical properties affected by the controlled hydrothermal preparation. The maximum loss at thickness of 2 mm is − 13 dB with 3 GHz bandwidth (< − 10 dB) for pure Ba-M ferrite and zero for substituted samples (Fig. 9a). Nearby, 2 GHz bandwidth for substituted samples with $x = 0.7$ and 0.9 is greater than − 10 dB for about 12 GHz at thickness of 2.5 mm, which is almost 3 GHz with maximum loss of − 26 dB for $x = 0$ (Fig. 9b). For the thickness of 3 mm, the reflection loss and effective bandwidth decrease for almost all samples (Fig. 9c). It is obvious that reflection loss intensity of all substituted samples has decreased compared to the pure sample at small thicknesses (2–3 mm), so substitution of a series of Gd-Mn-Co in Ba-M ferrite is not the best for development of radar absorbing material research and stealth coating technology, but can be useful for other lossy applications in microwave ranges. Also, there is a huge advance in reflective loss intensities of substituted samples in thickness of about 5.6 mm (Fig. 9d). The reflection loss peaks for $d = 5.6$ mm are effective at 5–6 and 16–17.5 GHz frequencies, which do not have any significant shifts for different concentrations of Gd, Mn and Co cations; this is related to a resonance due to absorbent dimensions. In this case, the loss intensity of sample $x = 0.5$ is − 48 dB at 17.2 GHz with bandwidth 2 GHz (< − 10 dB) and other samples have good results too, which are listed in Table IV. The frequency dependencies of the reflection loss of pure Ba-hexaferrite for different thicknesses from 2 to 3 by step of 0.2 mm in Fig. 10 shows that the effective bandwidth does not change by increasing the thickness, but the peak frequency have shift from 13 GHz to lower ones up to 10 GHz. As a

Table IV. Microwave characteristics of $Ba_{1-x}Gd_xFe_{12-2y}(MnCo)_yO_{19}$ for $y = \frac{x}{2}$ and $x = 0$–1

Samples	Matching frequency (GHz)	Reflection loss (dB)	Matching thickness (mm)	Bandwidth for losses greater than − 10 dB (GHz)
$x = 0.0$	11.8	− 26	2.5	3.2
$x = 0.1$	17.6	− 22	5.6	1.2
$x = 0.3$	17.5	− 24	5.6	0.9
$x = 0.5$	17.2	− 48	5.6	1.5
$x = 0.7$	12.2, 11.9, 17.5	− 15, − 13, − 30	2.5, 3, 5.6	2, 1.9, 1.8
$x = 0.9$	12, 16.8	− 14, − 22	2.5, 5.6	2, 2.2
$x = 1.0$	12.5, 11.9, 17.2	− 12, − 13, − 17	2.5, 3, 5.6	2.5, 2, 1.2

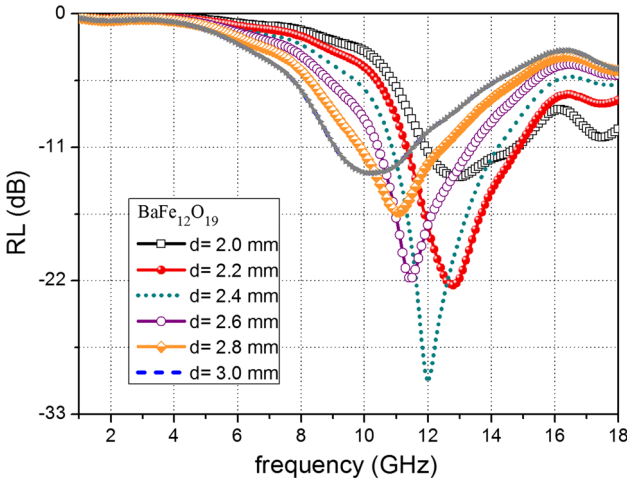

Fig. 10. The reflection loss curves for $BaFe_{12}O_{19}$ containing 70% ferrite synthesized by hydrothermal method with different absorber thicknesses from 2 mm to 3 mm.

result, it is useful to noted that a slight change in thickness can be used to control the frequency of absorption.

CONCLUSIONS

Nanoparticles Gd-Mn-Co substituted onto barium hexaferrite were successfully prepared by hydrothermal method. The range of particle size is about 62 nm to 85 nm with almost analogous morphology, which is suitable for signal-to-noise ratio. The magnetizations and coercivity values of substituted composites were decreased markedly at higher concentration of substitution compared to the undoped barium ferrite. The prepared composites structures were M-type hexagonal which confirmed by XRD studies and by calculation of cell constants and cell volume from XRD data. The maximum and remnant magnetizations decreased with increasing Gd-Mn-Co concentration in comparison with pure Ba-hexaferrite. The main reason for decreasing magnetizations was site occupation of Mn and Co ions. Also, crystal anisotropy, grain growth controlling and spin canting affected the coercivity. Reflection loss evaluations indicated that $Ba_{0.5}Gd_{0.5}Fe_{11}Mn_{0.5}Co_{0.5}O_{19}$ ferrite can act as an absorber due to a maximum RL of − 48 dB at 17.2 GHz with suitable bandwidth of 2 GHz less than − 20 dB.

REFERENCES

1. K. Rana, P. Thakur, A. Thakur, M. Tomar, and V. Gupta, *Ceram. Int.* 42, 8413 (2016).
2. G.B. Teh and R.D. Tilley, *J. SolGel Sci. Technol.* 77, 306 (2016).
3. R. Kaur, N. Dhillon, Ch Singh, S.B. Narang, and M. Chandra, *Solid State Commun.* 201, 72 (2015).
4. E.D. Solovyova, E.V. Pashkova, V.P. Ivanitski, O.I. V'yunov, and A.G. Belous, *J. Magn. Magn. Mater.* 330, 72 (2013).
5. J. Ding, X.Y. Liu, J. Wang, and Y. Shi, *Mater. Lett.* 44, 19 (2000).
6. A. Arab, M.R. Mardaneh, and M.H. Yousefi, *J. Magn. Magn. Mater.* 374, 80 (2015).
7. A. Nikzad, A. Ghasemi, M.K. Tehrani, and Gh.R. Gordani, *J. Supercond. Nov. Magn.* 29, 1657 (2016).
8. L.A. Garci and P.J. Reséndiz-Hernández, *J. Alloys Compd.* 369, 182 (2004).
9. W.C. Hsu, S.C. Chen, P.C. Kuo, C.T. Lie, and W.S. Tsai, *Mater. Sci. Eng. B* 111, 142 (2004).
10. M.J. Iqbal, M.N. Ashiq, and I.H. Gul, *J. Magn. Magn. Mater.* 322, 1720 (2010).
11. J. Huo and M. Wei, *Mater. Lett.* 63, 1183 (2009).
12. A. Xia, C. Zuo, L. Chen, C. Jin, and Y. Lv, *J. Magn. Magn. Mater.* 332, 186 (2013).
13. X. Yi, Q. Yitaia, L. Jinga, C. Zuyaoa, and Y. Li, *Mater. Sci. Eng. B* 34, L1 (1995).
14. S.K. Chawla, S.K. Chawla, R.K. Mudsainiyan, S.S. Meena, and S.M. Yusuf, *J. Magn. Magn. Mater.* 350, 23 (2014).
15. Z.W. Li, L. Chen, and C.K. Ong, *J. Appl. Phys.* 92, 3902 (2002).
16. M. Jamalian, A. Ghasemi, and M.J. Pourhosseini Asl, *J. Electron. Mater.* 44, 2856 (2015).
17. M.R. Meshram, N.K. Agrawal, B. Sinha, and P.S. Misra, *J. Magn. Magn. Mater.* 271, 207 (2004).
18. M. Mozaffari, A. Arab, M.H. Yousefi, and J. Amighian, *J. Magn. Magn. Mater.* 322, 2620 (2010).
19. M.N. Ashiq, S. Shakoor, M. Najam-ul-Haq, M.F. Warsi, I. Ali, and I. Shakir, *J. Magn. Magn. Mater.* 374, 173 (2015).
20. X. Batlle, M. Garcia del Muro, and J. Tejada, *J. Appl. Phys.* 74, 3333 (1993).
21. C. Singh, S.B. Narang, I.S. Hudiara, Y. Bai, and K. Marina, *Mater. Lett.* 63, 1921 (2009).
22. J. Zhao, R. Zhang, and Z. Fan, *Electr. Comput. Mater.* 26, 53 (2007).
23. M.A. Ahmed, N.G. Imam, M.K. Abdelmaksoud, and Y.A. Saeid, *J. Rare Earths* 33, 965 (2015).
24. J.S. Lee, J.M. Cha, H.Y. Yoon, J.K. Lee, and Y.K. Kim, *Sci. Rep.* 5, 12135 (2015).
25. G. Litsardakis, I. Manolakis, and K. Efthimiadis, *J. Alloys Compd.* 427m, 194 (2007).
26. S.W. Lee, S.Y. An, I.B. Shim, and C.S. Kim, *J. Magn. Magn. Mater.* 290, 231 (2005).
27. R.C. Pullar, *J. Magn. Magn. Mater.* 57, 1191 (2012).
28. A.M. Alsmadi, I. Bsoul, S.H. Mahmood, G. Alnawashi, F.M. Al-Dweri, Y. Maswadeh, and U. Welp, *J. Alloys Compd.* 648, 419 (2015).
29. I. Ali, M.U. Islam, I. Sadiq, N. Karamat, A. Iftikhar, M. Azhar khan, A. Shah, M. Athar, I. Shakir, and M.N. Ashiq, *J. Magn. Magn. Mater.* 385, 386 (2015).
30. G. Litsardakisa, I. Manolakisa, and C. Serletisb, *J. Magn. Magn. Mater.* 310, e884 (2007).
31. RSh Alam, M. Moradi, H. Nikmanesh, J. Ventura, and M. Rostami, *J. Magn. Magn. Mater.* 402, 20 (2016).
32. S.B. Narang and I.S. Hudiara, *J. Ceram. Proc. Res.* 7, 113 (2006).
33. P. Singh, V.K. Babbar, A. Razdan, S.L. Srivastava, V.K. Agrawal, and T.C. Goel, *J. Mater. Sci.* 41, 7190 (2006).
34. C.A. Stergiou, I. Manolakis, and T.V. Yioultsis, *J. Magn. Magn. Mater.* 322, 1532 (2010).
35. W. Jing, Z. Hong, B. Shuxin, C. Ke, and Z. Changrui, *J. Magn. Magn. Mater.* 312, 310 (2007).
36. S.B. Narang, K. Pubby, and C. Singh, *J. Electron. Mater.* 46, 718 (2017).
37. S.E. Jacobo, W.G. Fano, A.C. Razzitte, N.D. Digiovanni, and V. Trainotti, *Annual Report Conference on El. Insulation and Diel. Phenomena*, 1, 273 (1998).
38. S. Ounnunkad, *J. Solid State Commun.* 138n, 472 (2006).
39. X. Liu, W. Zhong, S. Yang, Z. Yu, B. Gu, and Y. Du, *Phys. Status Solidi (a)* 193, 314 (2002).
40. R.S. Alam, M. Moradi, M. Rostami, H. Nikmanesh, R. Moayedi, and Y. Bai, *J. Magn. Magn. Mater.* 381, 1 (2015).
41. J.R. Truedson, K.D. McKinstry, P. Kabos, and C.E. Patton, *J. Appl. Phys.* 74, 2705 (1993).
42. M.H. Shams, S.M.A. Salehi, and A. Ghasemi, *Mater. Lett.* 62, 1731 (2008).